Photoexcited Polaron Dynamics in Rutile TiO_2 from First-Principles On-the-Fly Surface Hopping

Chang Gao (高畅)[1], Qijing Zheng (郑奇靖)[1,2,3] and Jin Zhao (赵瑾)[1,2,4,5*]

[1]*ICQD/Hefei National Research Center for Physical Sciences at the Microscale, and Department of Physics, University of Science and Technology of China, Hefei, Anhui 230026, China*

[2]*Hefei National Laboratory, University of Science and Technology of China, Hefei, Anhui 230088, China*

[3]*State Key Laboratory of Precision and Intelligent Chemistry,University of Science and Technology of China, Hefei, Anhui, 230026, China*

[4]*Department of Physics and Astronomy, University of Pittsburgh, Pittsburgh, Pennsylvania 15260, United States*

[5]*College of Physics, Guizhou University, Guiyang City 550025, China*

Abstract

Photoinduced polaron dynamics challenges the classical path approximation (CPA), which prescribes nuclear motion on a single potential-energy surface (PES). To overcome this limitation, we use ΔSCF-based on-the-fly surface hopping involving both ground- and excited-state PESs to study photoexcited polaron dynamics in rutile TiO_2. The simulations capture electron and hole polaron formation, migration, recombination, and subsequent ultrafast lattice relaxation. The electron–hole recombination lifetime increases by approximately two orders of magnitude relative to CPA-NAMD, from 38 ps to 6.3 ns. This increase arises from reduced nonadiabatic coupling: excitation-induced electron redistribution substantially changes the orbitals relative to the ground state at the same nuclear geometry. These results highlight the importance of orbitals associated with both PESs and lattice feedback in electron–hole recombination. The approach provides a tool for investigating excited-state dynamics in solids where the CPA breaks down.

Keywords: photoexcited polarons; rutile TiO_2; nonadiabatic dynamics; on-the-fly surface hopping

Nonadiabatic molecular dynamics (NAMD) is increasingly used to investigate interfacial charge transfer, hot-carrier relaxation, and electron–hole recombination in solid-state materials. By resolving these processes at the atomic level, NAMD provides insight into charge and energy flow relevant to solar cells, optoelectronic devices, and photocatalysts.[1–14]

However, most NAMD simulations of solids adopt the classical path approximation (CPA): electronic dynamics is propagated along a prescribed nuclear trajectory, typically generated by ground-state ab initio molecular dynamics (AIMD).[15–17] Lattice motion thus affects electronic evolution, while electron excitions do not modify nuclear motion. This approximation can be justified when excitation-induced changes in nuclear motion are negligible, as may occur in stiff lattices, at low excitation densities, or when rapid electronic transitions among densely spaced levels limit the time available for structural relaxation on an individual state. It becomes inadequate, however, when electronic excitation drives structural changes, as in photoinduced phase transformations, surface photochemical reactions, and polaron formation. Describing these processes requires accounting for the feedback of electronic excitation on the lattice.[18–29]

Photoinduced polaron formation provides a direct example of this feedback, with carrier localization coupled to a stabilizing lattice distortion. Previous studies have incorporated this response by generating excited-state AIMD trajectories using the delta self-consistent field (ΔSCF) approach and subsequently propagating electronic dynamics along them.[27,28,30] Although this strategy uses ΔSCF to capture polaron formation, it still relies on a single potential energy surface (PES): the nuclei evolve on the excited-state PES, and the nonadiabatic couplings (NACs) are calculated solely from its Kohn–Sham orbitals. Electron–hole recombination, however, involves a transition between the excited- and ground-state PESs, requiring a coupling that incorporates the independently optimized orbitals associated with both PESs. Moreover, a prescribed excited-state trajectory cannot describe the change in nuclear forces upon recombination or the ensuing ground-state lattice relaxation. A surface-hopping description of the complete sequence therefore requires both PESs, their interstate coupling, and nuclear motion that responds to electronic transitions.[27,28]

Here, we combine a single-determinant ΔSCF description of electronic excitation with first-principles on-the-fly surface hopping to study photoinduced polaron dynamics in rutile TiO_2. We follow electron and hole polaron formation, hopping between lattice sites, recombination, and subsequent lattice relaxation. Compared with the CPA-based NAMD using a single PES, the calculated recombination timescale increases from 38 ps to 6.3 ns. Our analysis attributes this slower recombination to self-consistent orbital reorganization when the electron- and hole-polaron levels become close in energy, which reduces the average NAC magnitude associated with recombination from 1.5 to 0.2 meV. These results highlight the importance of including orbitals associated with both the ground- and excited-state PESs and nuclear feedback in describing polaron dynamics, connecting carrier localization to recombination and structural recovery within a unified framework.

The ground state is obtained from ground-state DFT, and the excited state from a fixed-occupation ΔSCF calculation in which one electron is promoted in the spin-up channel. Both states are represented by single Slater determinants. In a two-electron approximation, lower occupied orbitals are assumed to remain unchanged upon excitation, giving

$$\Phi_0 = |v^0 \uparrow\ v^0 \downarrow\rangle, \qquad \Phi_1 = |c^1 \uparrow\ v^1 \downarrow\rangle. \tag{1}$$

Each ket denotes a normalized determinant; v and c label the active valence and conduction orbitals, and the arrows denote their spin channels. Superscripts 0 and 1 denote orbitals obtained from ground-state DFT and excited-state ΔSCF calculations, respectively.

Because the two wave functions are optimized independently, they are not generally orthogonal. We therefore construct an orthonormal basis for electronic propagation. Using effective Hamiltonian $H_{01} = E_0 s$, the generalized eigenvalue problem yields the orthonormal wave functions and corresponding energies

$$\begin{aligned} \widetilde{\Phi}_0 &= \Phi_0, \widetilde{\Phi}_1 = \frac{\Phi_1 - s\Phi_0}{\sqrt{1-|s|^2}}, \\ \tilde{E}_0 &= E_0,\ \ \tilde{E}_1 = \frac{E_1 - |s|^2 E_0}{1-|s|^2}. \end{aligned} \tag{2}$$

Here, $s = \langle \Phi_0 | \Phi_1 \rangle$ is the dimensionless overlap of the original states at the same nuclear configuration, and E_0 and E_1 are the ground-state DFT and excited-state ΔSCF total energies. The time-derivative NAC is

$$d_{jk} = \left\langle \widetilde{\Phi}_j \left| \frac{\partial}{\partial t} \right| \widetilde{\Phi}_k \right\rangle, \qquad j,k \in \{0,1\}. \tag{3}$$

It is evaluated from finite differences of adjacent-time overlaps, constructed from KS orbital overlaps and transformed using Eq. (2). Electronic coefficients evolve according to $i\hbar \dot{C}_j = \tilde{E}_j C_j - i\hbar \sum_k d_{jk} C_k$, with decoherence and transitions treated using conventional decoherence-induced surface hopping (DISH).[31] Nuclear propagation and hop energy adjustments use the original total energies E_0, E_1 and their forces. This neglects the orthogonalization correction to the nuclear potential energy surfaces since the small state overlaps yield nearly coincident original and diagonalized energies along the sampled trajectory (see Supplemental Material).[32]

In KS-orbital-based NAMD within the CPA, the NAC evaluated using the excited-state orbitals is $d_{cv}^{\mathrm{KS}} = \langle c_\uparrow^1 | \frac{\partial}{\partial t} | v_\uparrow^1 \rangle$. By contrast, choosing the ground-state phase to satisfy the parallel-transport condition $\langle \Phi_0 | \frac{\partial}{\partial t} | \Phi_0 \rangle = 0$, Eqs. (1) and (2) give

$$d_{10} = \frac{1}{\sqrt{1-|s|^2}}\left[\left\langle c_{\uparrow}^{1}\left|\frac{\partial}{\partial t}\right|v_{\uparrow}^{0}\right\rangle\langle v_{\downarrow}^{1}|v_{\downarrow}^{0}\rangle + \langle c_{\uparrow}^{1}|v_{\uparrow}^{0}\rangle\left\langle v_{\downarrow}^{1}\left|\frac{\partial}{\partial t}\right|v_{\downarrow}^{0}\right\rangle\right]. \quad (4)$$

An excited-state ΔSCF nuclear trajectory is generated first, and both electronic states and their NACs are subsequently evaluated along it. The equilibrated NVE trajectory is reused repeatedly to sample long-time recombination dynamics.[33,34] Upon an accepted hop to the ground state, the configuration and velocity are taken from the corresponding segment, all nuclear velocities are uniformly rescaled to conserve $K_{\mathrm{nuc}} + E_a$,[35] and a new ground-state AIMD trajectory is initiated. Thus, the nuclear path responds to recombination rather than continuing along the prescribed excited-state trajectory.

The present implementation is limited to a two-state description and is most suitable for well-separated electronic states whose transitions induce appreciable changes in nuclear motion. Dense excited-state manifolds with strong state mixing or near-degeneracies may hinder ΔSCF convergence and state tracking, and frequent hops may require more rigorous momentum adjustments. Extension to multistate or strongly multiconfigurational systems will require further methodological development.

Electronic-structure calculations and AIMD were performed using VASP with the projector augmented-wave method and PBE+U.[36–39] A $2 \times 2 \times 3$ rutile TiO_2 supercell was used, with $U = 3.5$ eV for Ti 3d and $U = 6.5$ eV for O 2p orbitals.[28,40] The U values were chosen by comparing the optimized lattice structures and calculated electronic structures with HSE results (see Supplemental Material). NVT equilibration at 300 K preceded NVE sampling. Electronic dynamics was simulated using Hefei-NAMD,[6] reusing a 4 ps NVE segment with 100 realizations for each of five initial nuclear configurations, giving 500 realizations in total.

The lifecycle of photoinduced polarons in rutile TiO_2 begins with electronic excitation, followed by lattice relaxation toward a local minimum on the excited-state potential energy surface and the concomitant self-trapping of carriers. After a period of polaron evolution, electron–hole recombination returns the system to the ground-state surface, where the lattice relaxes back to its equilibrium minimum. Figure 1 summarizes this sequence through four representative states (A–D). The corresponding densities of states (DOS) and orbital distributions are shown in Figs. 1(A)–1(D), while Fig. 1(E) illustrates the potential energy surfaces and total-energy differences. Starting from the equilibrium ground state A, vertical photoexcitation produces state B at the same nuclear configuration. Subsequent relaxation on the excited-state surface (process I, B→C) localizes the electron and hole on Ti and O sites, respectively, accompanied by lattice distortion and the emergence of polaron levels within the band gap. This relaxation lowers the excited-state total energy by 0.085 eV. Electron–hole recombination then returns the system to the ground-state surface (process II, C→D), with a total-energy difference of 1.008 eV at the distorted configuration shown. Although the excited carriers have recombined in D, the lattice retains the polaron-induced distortion, and the band-edge orbitals remain spatially localized. Subsequent ground-state structural relaxation

(process III, D→A) removes this residual distortion and restores the equilibrium electronic structure, lowering the potential energy by a further 1.058 eV.

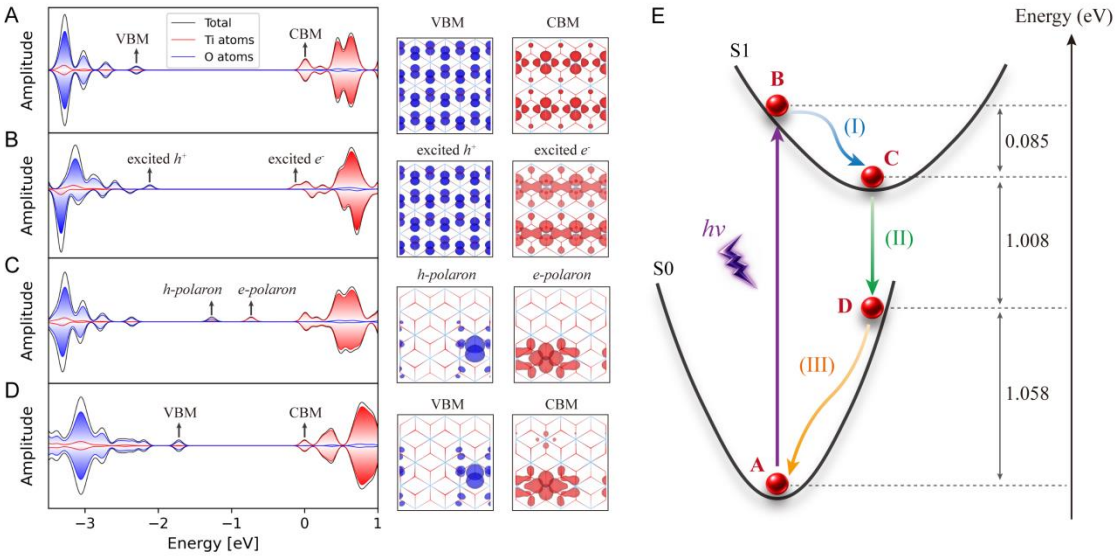

Figure 1. Polaron formation and recombination in rutile TiO_2. (A–D) DOS and orbital distributions before excitation (A), immediately after excitation (B), after polaron formation (C), and immediately after recombination (D). (E) Schematic potential energy surfaces showing polaron formation (I), recombination (II), and lattice recovery (III), with total-energy differences indicated.

We follow a representative trajectory to examine polaron formation, subsequent evolution, and recombination. Figure 2(A, B) resolves the initial formation of photoexcited small polarons through the time evolution of the carrier-associated KS levels, local bond lengths, and orbital distributions. During the first 35 fs after excitation, the electron level decreases to a local minimum [Fig. 2(A)], while the average Ti–O bond length around the Ti site hosting the electron increases to a local maximum [Fig. 2(B)]. The orbital distribution at 35 fs [Fig. 2(A)] further shows the formation of a localized electron polaron. Hole localization follows during 47–96 fs: the hole-associated level rises to a local maximum, accompanied by an increase in the average Ti–O bond length around the O site hosting the hole to near its maximum. The orbital distribution at 96 fs confirms the formation of a localized hole polaron. These correlated changes in electronic localization and local lattice distortion identify sequential electron and hole polaron formation along the illustrated trajectory.

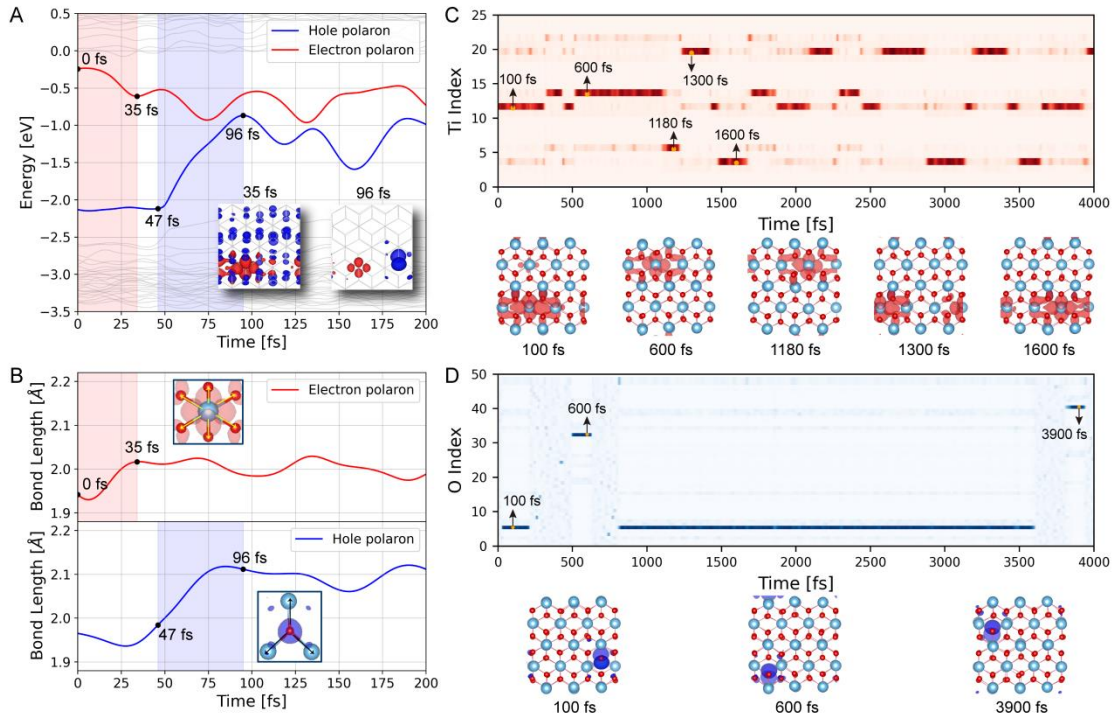

Figure 2. Polaron formation and spatial evolution along a representative trajectory. (A) Electron- and hole-associated KS levels (red and blue). Insets show electron (red) and hole (blue) orbital distributions at selected times. (B) Average Ti–O bond lengths around the electron- and hole-localization sites (upper and lower panels). Shading marks the formation intervals; insets show local coordination. (C, D) Spatial evolution along the trajectory. Orbital weights on Ti sites for the electron (C) and O sites for the hole (D); darker colors indicate larger weights. Snapshots below show orbital distributions at the marked times.

Following polaron formation, we track the spatial distributions of the electron and hole along the same trajectory [Fig. 2(C, D)]. The electron polaron frequently hops between different Ti sites [Fig. 2(C)]. In contrast, the hole alternates between localized and delocalized states, with relocalization potentially occurring at a different O site [Fig. 2(D)]. The representative orbital distributions illustrate these distinct modes of carrier motion. The intermittent hole localization is consistent with an activated self-trapping process: formation of the hole polaron requires overcoming a barrier of approximately 0.08 eV (see Supplemental Material).

We next investigate electron–hole recombination using the NACs in on-the-fly surface hopping and compare the results with KS-orbital-based NAMD within the CPA. Figure 3(A) compares the NACs over a 4 ps segment of this representative trajectory, showing a reduction of approximately one to two orders of magnitude in the on-the-fly treatment. The NAC magnitudes averaged over the 500 trajectories are 1.5 meV for the CPA treatment and 0.2 meV for on-the-fly surface hopping. The much weaker coupling is accompanied by substantially slower recombination: exponential fits to the excited-state populations averaged over 500 trajectories yield a lifetime of approximately 6.3 ns for

on-the-fly surface hopping [Fig. 3(B)], compared with 38 ps for the CPA treatment [Fig. 3(C)].

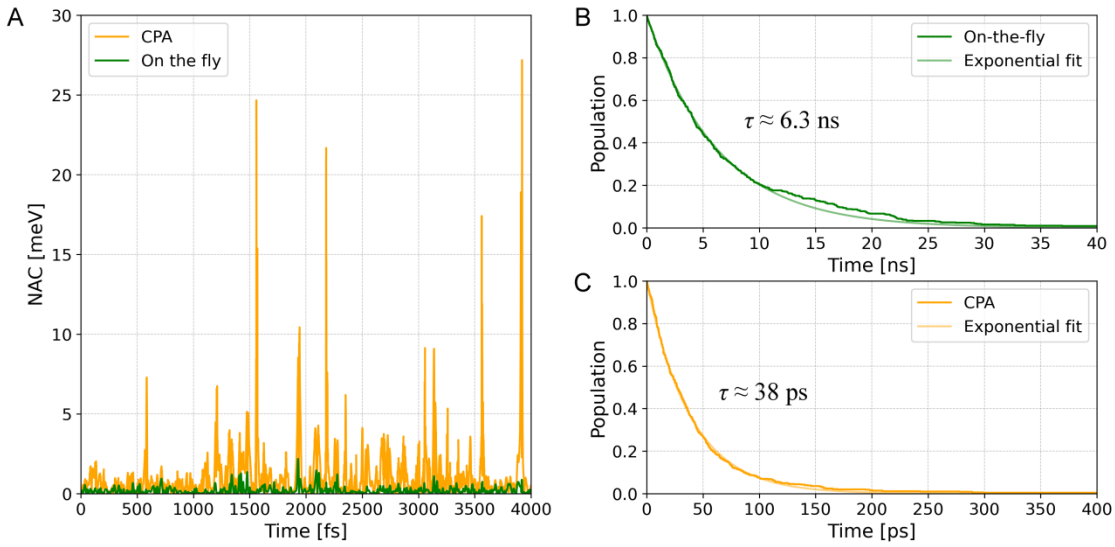

Figure 3. NACs and recombination dynamics. (A) On-the-fly and CPA coupling magnitudes over a 4 ps segment of the trajectory in Figs. 2. (B, C) Excited-state populations averaged over 500 trajectories and exponential fits for on-the-fly surface hopping (B) and CPA (C). Note the different time units.

Returning to the same representative trajectory, Fig. 4 illustrates the structural response to a hop to the ground state at t_0=3.73 ns. Figure 4(A) shows the ground- and excited-state potential energies along the nuclear trajectory, which follows the excited-state surface before the hop and the ground-state surface afterward. Within approximately 11 fs after recombination, the polaron-associated in-gap levels merge into the band edges [Fig. 4(B)]. The accompanying lattice recovery occurs more slowly: the average Ti–O bond lengths around the former electron- and hole-localization sites contract, reaching their first post-hop minima at approximately 22 and 34 fs, respectively [Fig. 4(C, D)]. Subsequent bond-length oscillations reflect the continuing lattice motion on the ground-state surface. These results resolve the rapid electronic and structural response following the much slower recombination process.

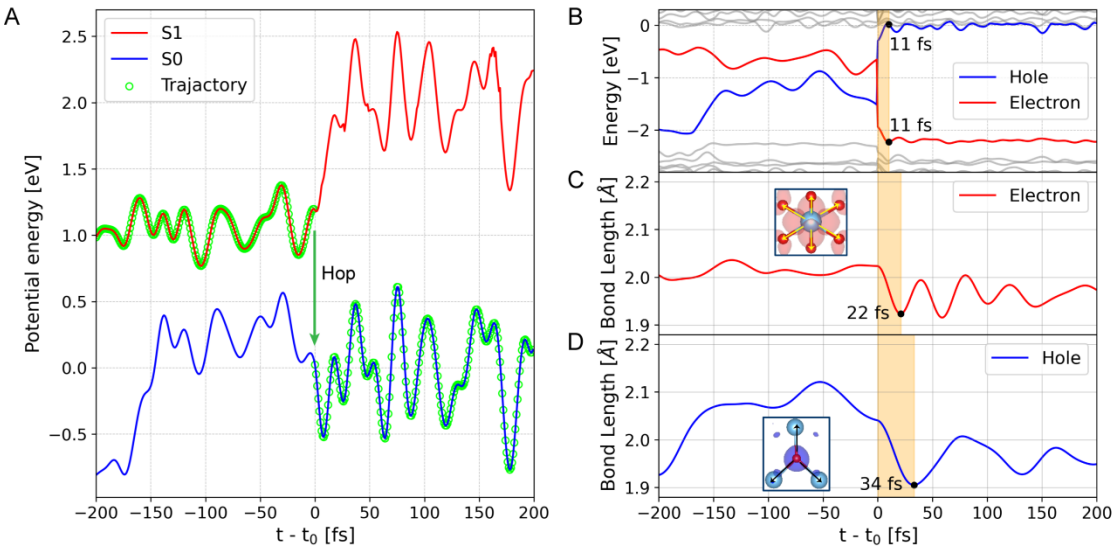

Figure 4. Recombination and relaxation along the same representative trajectory, with time relative to the hop at $t_0 = 3.73$ ns. (A) Ground- and excited-state potential energies; green circles mark the active surface. (B) Polaron-associated KS levels. (C) Average Ti–O bond lengths around the former electron- and hole-localization sites (upper and lower panels). Shading marks the indicated response times.

Using ΔSCF-based on-the-fly surface hopping, we follow polaron formation, migration, and eventual electron–hole recombination in rutile TiO_2. The electron-polaron formation and migration behavior is broadly consistent with previous studies.[27,28] A notable difference is the formation of a hole polaron in the present simulations. We attribute this primarily to the inclusion of a Hubbard correction on O 2p states, guided by comparison with HSE calculations, which enables a description of hole localization and the associated lattice distortion.[24,40,41] By explicitly propagating the nuclei on the active electronic potential-energy surface and allowing transitions between the excited and ground states, our simulations also resolve the lattice response to recombination, which is missing in previous studies.

The most pronounced difference from the CPA-NAMD calculations is the polaron lifetime, which increases by approximately two orders of magnitude in the present simulations. The resulting electron–hole recombination timescale is closer to the nanosecond-scale carrier lifetimes reported experimentally for rutile TiO_2 single crystals,[42] although experimental lifetimes depend on sample conditions and excitation density. This longer polaron lifetime arises primarily from evaluating the NAC using two independently optimized sets of orbitals, one for the ground state and the other for the ΔSCF excited state. As derived in Eq. (4), when the two electronic states are constructed from the same orbital set, the second term vanishes and the first reduces exactly to the single-PES coupling used in the CPA treatment, $d_{cv}^{\mathrm{KS}} = \langle c_{\uparrow}^{1} | \partial / \partial t | v_{\uparrow}^{1} \rangle$. Independently optimizing the ground-state and ΔSCF orbitals changes this coupling substantially. Although the first term in Eq. (4) remains dominant, both the contribution involving time-displaced overlaps between the ground-state VBM and the ΔSCF CBM and the overlap between the independently optimized ground-state and ΔSCF excited-state VBM orbitals, v^0 and v^1, are reduced. This overlap between v^0 and v^1 is evaluated at the same

nuclear geometry; it therefore reflects the change in the VBM orbital upon electronic excitation at fixed geometry. If the orbital remains unchanged upon excitation, the magnitude of this overlap is 1.0. At polaronic geometries, its magnitude decreases to approximately 0.3 (see Supplemental Material). Together, these effects reduce the average NAC from 1.5 to 0.2 meV.

The key distinction is whether the NAC is calculated using orbitals from a single PES or from both the ground- and excited-state PESs. Within the CPA treatment considered here, the NAC is calculated between KS orbitals on the excited-state PES and reflects the electron–phonon coupling on that PES through lattice-induced orbital mixing. In TiO_2, strong electron–phonon coupling on the excited-state PES drives electron and hole polaron formation and can give rise to a large CPA-NAC. Electron–hole recombination, however, involves two different PESs, and electron–phonon coupling on the ground-state PES is much weaker in this system. Accurately describing recombination therefore requires orbitals from both PESs; using only the excited-state PES and its associated orbitals is insufficient. In the present system, the substantial reorganization accompanying polaron formation modifies both the inter-state overlap and its time dependence, strongly suppressing the recombination coupling.

ΔSCF-based on-the-fly surface hopping has been developed for molecules but, to our knowledge, has not been applied to periodic solids.[43,44] Zhang et al. incorporated excited-state forces and full nonadiabatic coupling vectors into machine-learning-assisted on-the-fly surface hopping in solids,[45] while explicitly neglecting the self-consistent response of the electronic Hamiltonian to the excited charge density. This approximation may affect the calculated couplings when the orbitals differ substantially between the ground- and excited-state PESs. The present approach provides a practical framework for capturing both lattice feedback and the effects of independently optimized orbitals associated with the ground- and excited-state PESs on nonadiabatic couplings. It is particularly suited to semiconductors with sufficiently separated and identifiable electronic states, including band-edge excitations and sparse defect levels. Potential applications include photoinduced structural changes, defect-mediated recombination, and selected processes in molecular crystals and surface photocatalysis, provided that the relevant states can be represented and tracked within ΔSCF.

Acknowledgements Jin Zhao acknowledges support from the National Key Research and Development Program of China (Grant No. 2024YFA1409800), the National Natural Science Foundation of China (Grants No. 12125408 and No. 12334004), and New cornerstone Science Foundation through the XPLORER PRIZE.

References

[1] Akimov A V, Asahi R, Jinnouchi R, and Prezhdo O V 2015 *J. Am. Chem. Soc.* **137** 11517

[2] Chu W, Saidi W A, Zheng Q, Xie Y, Lan Z, Prezhdo O V, Petek H, and Zhao J 2016 *J. Am. Chem. Soc.* **138** 13740

[3] Long R, Fang W H, and Prezhdo O V 2017 *J. Phys. Chem. C* **121** 3797

[4] Zhang J, Hong H, Lian C, Ma W, Xu X, Zhou X, Fu H, Liu K, and Meng S 2017 *Adv. Sci.* **4** 1700086

[5] Li W, Tang J, Casanova D, and Prezhdo O V 2018 *ACS Energy Lett.* **3** 2713

[6] Zheng Q, Chu W, Zhao C, Zhang L, Guo H, Wang Y, Jiang X, and Zhao J 2019 *WIREs Comput. Mol. Sci.* **9** e1411

[7] Liu X Y, Chen W K, Fang W H, and Cui G 2019 *J. Phys. Chem. Lett.* **10** 2949

[8] Zhang L, Vasenko A S, Zhao J, and Prezhdo O V 2019 *J. Phys. Chem. Lett.* **10** 1083

[9] Chu W, Saidi W A, Zhao J, and Prezhdo O V 2020 *Angew. Chem. Int. Ed.* **59** 6435

[10] Smith B, Shakiba M, and Akimov A V 2021 *J. Phys. Chem. Lett.* **12** 2444

[11] You P, Lian C, Chen D, Xu J, Zhang C, Meng S, and Wang E 2021 *Nano Lett.* **21** 6449

[12] Chu W, Tan S, Zheng Q, Fang W, Feng Y, Prezhdo O V, Wang B, Li X Z, and Zhao J 2022 *Sci. Adv.* **8** eabo2675

[13] Lu H, Fang W H, and Long R 2022 *J. Phys. Chem. Lett.* **13** 3016

[14] Cheng C, Prezhdo O V, Long R, and Fang W H 2022 *J. Am. Chem. Soc.* **145** 476

[15] Craig C F, Duncan W R, and Prezhdo O V 2005 *Phys. Rev. Lett.* **95** 163001

[16] Fischer S A, Duncan W R, and Prezhdo O V 2009 *J. Am. Chem. Soc.* **131** 15483

[17] Akimov A V and Prezhdo O V 2013 *J. Chem. Theory Comput.* **9** 4959

[18] Li X B, Liu X Q, Liu X, Han D, Zhang Z, Han X D, Sun H B, and Zhang S B 2011 *Phys. Rev. Lett.* **107** 015501

[19] Di Valentin C and Selloni A 2011 *J. Phys. Chem. Lett.* **2** 2223

[20] Gali A, Simon T, and Lowther J E 2011 *New J. Phys.* **13** 025016

[21] Bang J, Wang Z, Gao F, Meng S, and Zhang S B 2013 *Phys. Rev. B* **87** 205206

[22] Jia Y, Miglio A, Poncé S, Gonze X, and Mikami M 2016 *Phys. Rev. B* **93** 155111

[23] Paillard C, Xu B, Dkhil B, Geneste G, and Bellaiche L 2016 *Phys. Rev. Lett.* **116** 247401

[24] Zhang J, Peng C, Wang H, and Hu P 2017 *ACS Catal.* **7** 2374

[25] Lin M F, Kochat V, Krishnamoorthy A, Bassman Oftelie L, Weninger C, Zheng Q, Zhang X, Apte A, Tiwary C S, Shen X, Li R, Kalia R, Ajayan P, Nakano A, Vashishta P, Shimojo F, Wang X, Fritz D M, and Bergmann U 2017 *Nat. Commun.* **8** 1745

[26] Si C, Choe D, Xie W, Wang H, Sun Z, Bang J, and Zhang S 2019 *Nano Lett.* **19** 3612

[27] Zhang L, Chu W, Zhao C, Zheng Q, Prezhdo O V, and Zhao J 2021 *J. Phys. Chem. Lett.* **12** 2191

[28] Gao C, Zhang L, Zheng Q, and Zhao J 2021 *J. Phys. Chem. C* **125** 27275

[29] Wu S, Ma J, Zhang C, Prezhdo O V, Zhao J, Gong X G, and Chu W 2025 *J. Am. Chem. Soc.* **147** 21060

[30] Cheng C, Zhu Y, Zhou Z, Long R, and Fang W H 2022 *npj Comput. Mater.* **8** 148

[31] Jaeger H M, Fischer S, and Prezhdo O V 2012 *J. Chem. Phys.* **137** 22A545

[32] Doltsinis N L and Marx D 2002 *Phys. Rev. Lett.* **88** 166402

[33] Li L, Long R, Bertolini T, and Prezhdo O V 2017 *Nano Lett.* **17** 7962

[34] Li L, Long R, and Prezhdo O V 2018 *Nano Lett.* **18** 4008

[35] Mai S, Marquetand P, and González L 2020 Surface hopping molecular dynamics in *Quantum chemistry and dynamics of excited states* ed González L and Lindh R (Hoboken, NJ: John Wiley & Sons) p 499

[36] Kresse G and Furthmüller J 1996 *Phys. Rev. B* **54** 11169

[37] Blöchl P E 1994 *Phys. Rev. B* **50** 17953

[38] Anisimov V I, Zaanen J, and Andersen O K 1991 *Phys. Rev. B* **44** 943

[39] Dudarev S L, Botton G A, Savrasov S Y, Humphreys C J, and Sutton A P 1998 *Phys. Rev. B* **57** 1505

[40] Wang D, Wang H, and Hu P 2015 *Phys. Chem. Chem. Phys.* **17** 1549

[41] Zhou M, Chen D, Liu Y, and Wang H 2024 *Nat. Commun.* **15** 8744

[42] Yamada Y and Kanemitsu Y 2012 *Appl. Phys. Lett.* **101** 133907

[43] Pradhan E, Sato K, and Akimov A V 2018 *J. Phys.: Condens. Matter* **30** 484002

[44] Mališ M, Vandaele E, and Luber S 2022 *J. Chem. Theory Comput.* **18** 4082

[45] Zhang C, Zhong Y, Tao Z G, Li Y, Lan Z, Prezhdo O V, Gong X G, Chu W, and Xiang H 2026 *Phys. Rev. Lett.* **137** 076905